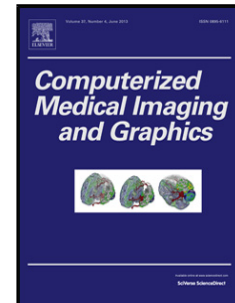# Accepted Manuscript

Title: Skin Lesion Image Segmentation Using Delaunay Triangulation for Melanoma Detection

Author: Andrea Pennisi Domenico D. Bloisi Daniele Nardi Anna Rita Giampetruzzi Chiara Mondino Antonio Facchiano
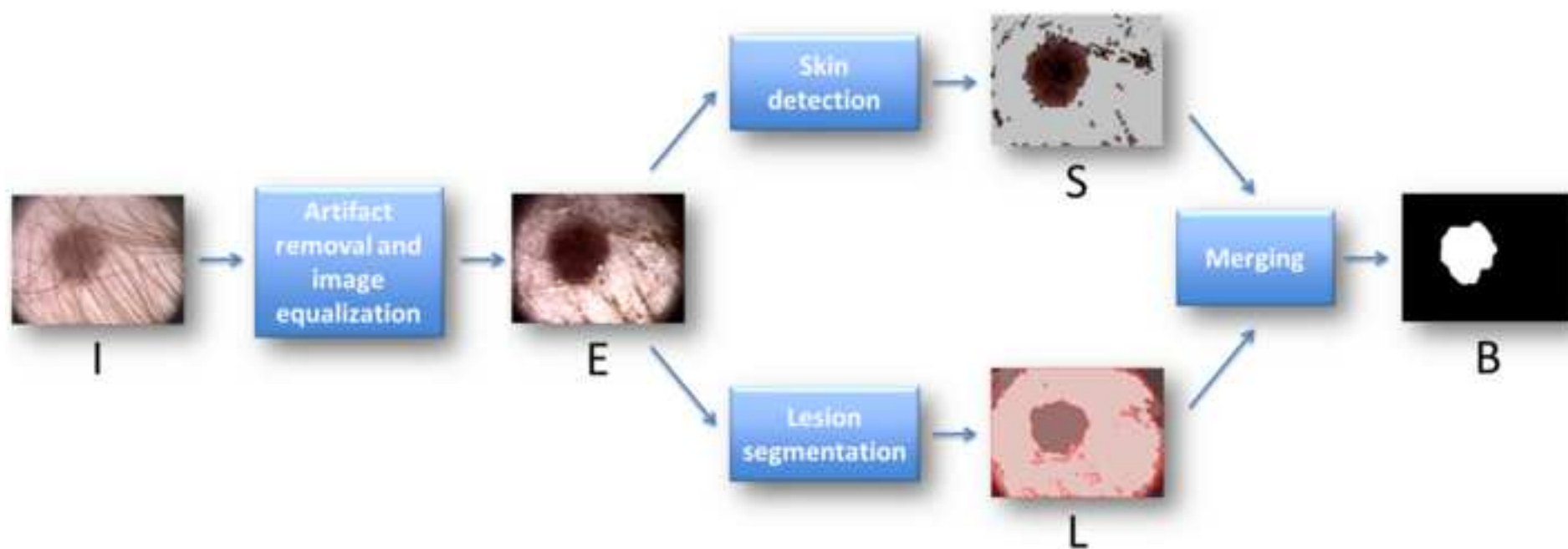
Please cite this article as: Andrea Pennisi, Domenico D. Bloisi, Daniele Nardi, Anna Rita Giampetruzzi, Chiara Mondino, Antonio Facchiano, Skin Lesion Image Segmentation Using Delaunay Triangulation for Melanoma Detection, <![CDATA[*Computerized Medical Imaging and Graphics*]]> (2016), http://dx.doi.org/10.1016/j.compmedimag.2016.05.002

Highlights

- An accurate and fully-automatic method for skin lesion segmentation is proposed.
- Skin detection and Delaunay Triangulation are used for finding the lesion area.
- A publicly available data set of dermoscopic images is used for the experiments.
- Very accurate segmentation results can be obtained for common and atypical nevi.
- Classification experiments achieved a sensitivity of 93.5%.

Skin Lesion Image Segmentation Using Delaunay Triangulation for Melanoma Detection

Andrea Pennisi[a,b], Domenico D. Bloisi[a,*], Daniele Nardi[a], Anna Rita Giampetruzzi[c], Chiara Mondino[c,d], Antonio Facchiano[c]

[a]*Department of Computer, Control, and Management Engineering, Sapienza University of Rome, via Ariosto 25, Rome, Italy*
[b]*Department of Electronics and Informatics Vrije Universiteit Brussel Pleinlaan 2 - B-1050 Brussel (Belgium)*
[c]*Istituto Dermopatico dell'Immacolata IDI-IRCCS, via Monti di Creta 104, Rome, Italy*
[d]*Department of Dermatology (Service of Allergology and Clinical Immunology), Cantonal Hospital of Bellinzona, 6500 Bellinzona, Switzerland*

Abstract

Developing automatic diagnostic tools for the early detection of skin cancer lesions in dermoscopic images can help to reduce melanoma-induced mortality. Image segmentation is a key step in the automated skin lesion diagnosis pipeline. In this paper, a fast and fully-automatic algorithm for skin lesion segmentation in dermoscopic images is presented. Delaunay Triangulation is used to extract a binary mask of the lesion region, without the need of any training stage. A quantitative experimental evaluation has been conducted on a publicly available database, by taking into account six well-known state-of-the-art segmentation methods for comparison. The results of the experimental analysis demonstrate that the proposed approach is highly accurate when dealing with benign lesions, while the segmentation accuracy significantly decreases when melanoma images are processed. This behavior led us to consider geometrical and color features extracted from the binary masks generated by our algorithm for classification, achieving promising results for melanoma detection.

Keywords: Melanoma detection, Dermoscopy images, Automatic segmentation, Border detection

*Corresponding author
Email address: bloisi@diag.uniroma1.it (Domenico D. Bloisi)

1. Introduction

Melanoma is one of the most aggressive tumors in humans [1] and it can be lethal, if not diagnosed on time. The incidence of melanoma among all dermatologic cancers is 4%, while melanoma-induced mortality accounts for about 80% of deaths from skin cancer; only 14% of patients with metastatic melanoma survive for five years [2]. Moreover, malignant melanoma has a cure rate of more than 95% if detected at an early stage [3]. The above statistics demonstrate that there is an urgent need to develop innovative strategies able to increase the diagnostic accuracy and to help dermatologists making early diagnosis. Indeed, given the current lack of effective therapeutic approaches, the early diagnosis is the main way to achieve a real impact on mortality from melanoma.

Novel approaches are being developed to help early diagnosis according to bio-physics analyses [4], molecular targets identifications [5], and novel image analysis criteria [6, 7]. In particular, the development of robust and reliable image analysis tools can reduce the number of presumptive diagnoses that have to be confirmed histologically on skin biopsy. Dermoscopy is one of the most important tool in the early diagnosis of melanoma. Dermoscopic images are obtained by combining optical magnification with either cross-polarized lighting or liquid immersion, with a low angle-of-incidence lighting. The use of dermoscopy gives a magnification of the images of the nevus lesions and it allows for the analysis of particular characteristics of the lesion, including symmetry, size, borders, presence and distribution of color features.

The typical computer-aided diagnosis (CAD) pipeline for automated skin lesion diagnosis (ASLD) from digital dermoscopic images can be subdivided into the following steps [8]:

1. Image acquisition;
2. Noise and artifact filtering;
3. Lesion segmentation;
4. Feature extraction;
5. Classification.

The lesion segmentation step is fundamental in order to increase the effectiveness of the subsequent steps, since it strongly affects the results of the whole pipeline [9]. Indeed, an accurate segmentation allows for deriving
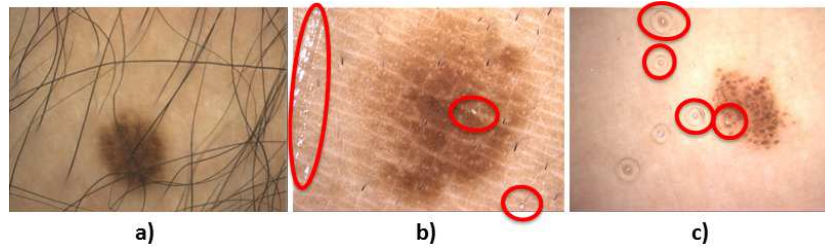
2

Figure 1: Difficulties in lesion segmentation on dermoscopic images. a) Presence of hair. b) Reflections. c) Air/oil bubbles. Images are from the PH^2 database [11, 12].

border structure information, such as the asymmetry and the irregularity of the lesion area, which are essential for a correct presumptive diagnosis. Furthermore, important clinical features like blue-white areas, atypical pigment networks, and globules can be automatically extracted only when the accuracy of the detected lesion border is high [10]. However, the great variety of lesion shapes, size and colors, the different skin types and textures, as well as the possible presence of hair and air/oil bubbles make segmentation a hard task (three examples of typical challenges are shown in Fig. 1).

In this paper, we describe a fully-automatic lesion segmentation method, able to process dermoscopic images even when reflections, oil bubbles, hairs or other imperfections are present, extending the work presented in [13]. The proposed algorithm, called ASLM, does not require any training stage and comprises four steps: (i) artifact removal; (ii) skin detection and (iii) lesion segmentation, which generate two different images containing the detected lesion region; and (iv) a final stage where a binary mask is obtained by merging those images. In particular, ASLM is designed to be sensitive with respect to images containing irregular borders, multiple shades of pigmentation, and varying texture. This is demonstrated by experimental results, carried out on the publicly available PH^2 database [11, 12], showing that the accuracy of the segmentation by ASLM is extremely high when dealing with benign lesions (common and atypical nevi), while the precision of the segmentation results significantly decreases when malignant lesions (melanoma) are analyzed. This behavior led us to consider the use of the binary masks generated by ASLM as input for a classification stage. The results for melanoma detection, obtained by considering only three geometrical features and three 16-bin color histograms, achieved 93.5% sensitivity and 87.1% specificity on a set of 200 dermoscopic images, demonstrating that ASLM can be a suitable

3

tool for the development of CAD support systems for the early detection of malignant lesions.

The remainder of the paper is organized as follows. Related work is discussed in Section 2, while the details of the proposed skin lesion segmentation method are presented in Section 3. The description of the data set used for the experiments as well as a quantitative comparison of our method with six well-known segmentation algorithms are given in Section 4. Melanoma detection is discussed in Section 5 and conclusions are drawn in Section 6.

2. Related Work

Automatic segmentation in dermoscopic images presents many difficulties related to the possible presence of hair, specular reflections, multiple colored lesion, low contrast between the lesion area and the surrounding skin, irregular and fuzzy lesion borders, and artifacts such as skin lines, blood vessels and air bubbles caused by dermoscopic gel [14]. Several segmentation algorithms have been proposed in the literature to deal with the problem of accurately segmenting skin lesion images and two surveys in this field have been realized by Celebi *et al.* [14, 15]. According to Xie and Bovick [9] and to Silveira *et al.* [16], existing approaches can be grouped into three main categories:

Thresholding methods. Approaches in this category aim at comparing visual feature values for single or group of pixels in the dermoscopic image with threshold values (e.g., a pixel is labelled as a lesion point if it is darker than a given color threshold value). The output of the thresholding process is a binary image, which can be further processed to filter out outliers, to fill small holes, or to select the largest connected component. Examples of thresholding methods are adaptive thresholding [17], histogram thresholding [18], and clustering. In particular, a clustering-based segmentation method for dermoscopy images is described in [19], where K-means++ (KPP), a variation of the standard k-means algorithm with random seeding, is used.

Different thresholding methods can be combined together. In [20], pixel-based and region-based methods are used in combination with a region-growing approach for automatically extracting the lesion area. In [10], the results generated by an ensemble of different thresholding methods are fused together, thus obtaining a final mask that exploits the peculiarities of each

4

specific method. In particular, four techniques are considered for constructing the ensemble: fuzzy similarity, maximum entropy, minimum error thresholding, and Otsu's clustering.

Thresholding methods performs well if there is a high contrast between the lesion area and the surrounding skin region, otherwise the segmentation accuracy can decrease. Moreover, thresholding methods can fail when processing images with significant amount of hair or air/oil bubbles [10].

Edge and contour-based methods. Algorithms in this group aim at identifying the discontinuities (i.e., the edges) in the dermoscopic images to detect the lesion borders. For example, an active contour method, which is based on gradient vector flow (GVF) snakes for contour extraction, is described in [21]. An extension of GVF based on mean shift (MSGVF) is proposed in [22]. Two contour based methods are applied to skin lesion images in [16], namely adaptive snake and active contour by level set. In the adaptive snake algorithm, detailed in [23], edge points are first grouped in strokes and then each stroke is classified as valid or not. A confidence level is associated to each stroke and the Expectation-Maximization (EM) algorithm is used to update the confidence levels and to estimate the object contour. The active contour by level set method, illustrated in [24], creates a model of the contour that does not exploit any edge detection function to stop the evolving curve on the boundary, but uses instead a stopping term based on Mumford-Shah segmentation techniques.

Edge and contour-based methods usually fail in presence of hair or air bubbles and if the transition between the lesion and the surrounding skin is smooth.

Region-based methods. This category includes algorithms working at a global image level. The basic assumption is that the image in input contains always two different regions: lesion and skin. A method called JSEG [25], based on color quantization and spatial segmentation, has been applied to skin lesion images in [8]. JSEG uses J-images, corresponding to measurements of local homogeneities at different scales, to find potential boundary locations. The final segmentation is obtained by growing regions from seed areas of the J-images. Statistical region merging (SRM) [26] is used in [27]. SRM treats the image as an observed instance of an unknown theoretical image, whose statistical regions are to be reconstructed.

Region-based algorithms are prone to over-segmentation when the skin

5

Figure 2: Skin lesion segmentation. a) Dermoscopic image in input. b) Binary mask in output. Images are from the PH^2 database [11, 12].

or lesion regions are textured or when the interior of the lesion exhibit multi-colored areas.

From the analysis of the literature it can be noted that:

- Existing solutions are reliable only when the dermoscopic image shows a high contrast between the lesion area and the surrounding skin region, the color intensity values inside the lesion area are uniform, and no artifacts are present. As an example, region based algorithms, like JSEG, tends to over-segment the lesion area.

- Segmentation results are in most cases obtained by using data sets that are not publicly available, thus making it difficult to perform a quantitative comparison with related work.

In this paper, a novel region-based, fully-automatic, and fast segmentation algorithm for skin lesion segmentation is presented. The proposed method can deal with the presence of hair, reflections, air/oil bubbles and it has been experimentally validated on a publicly available database of dermoscopic images. As a difference with previous work, we compute two parallel processes of skin detection and lesion segmentation and then merge the results, thus obtaining an accurate representation of the lesion area. The functional architecture of our approach is described in the next section along with the details of the four main functions, i.e., noise removal, skin detection, lesion segmentation, and merging.

3. Skin Lesion Segmentation

Given a dermoscopic image (Fig. 2a), the goal of the skin lesion segmentation process is to generate a binary mask providing an accurate separation

6

156 between the lesion area and the surrounding healthy skin (Fig. 2b). The
157 mask can be used for extracting information about the lesion border.

158 We propose an approach called ASLM that is shown in Fig. 3 and is
159 structured in four steps:

160 1. **A**rtifact removal and image equalization;

161 2. **S**kin detection;

162 3. **L**esion segmentation;

163 4. **M**erging.

164 In the first step, outliers are removed by morphological closing and the im-
165 age contrast is enhanced by equalization. Then, two segmentation processes
166 (steps 2 and 3) are carried out in parallel, yielding two different images. The
167 first one is built by detecting the skin region and then filtering it out. The
168 second image is created by applying edge detection and Delaunay Triangu-
169 lation. In the final step, the final lesion area is extracted by combining the
170 two images generated in steps 2 and 3.

171 As shown in Fig. 3, the dermoscopic image I in input is processed to re-
172 move artifacts (e.g., hair) and then equalized to produce an image E, which
173 represents the input for both the skin detection and the lesion segmentation
174 modules. The former generates an image S (called *skin image*) by using a
175 color thresholding mechanism, while the latter uses the Delaunay Triangula-
176 tion to create an image L (called *lesion image*), which contains the different
177 color regions in E. During the merging step, S and L are analysed for possi-
178 bly fusing adjacent regions, obtaining the final binary image B. The details
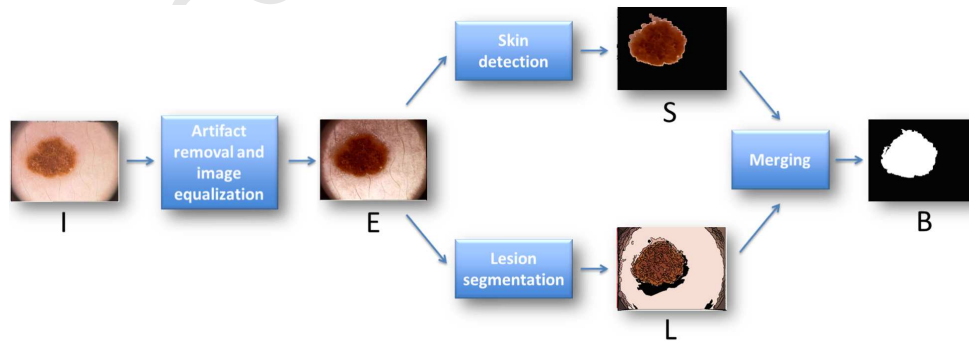179 about the above sketched steps are given in the rest of this section.

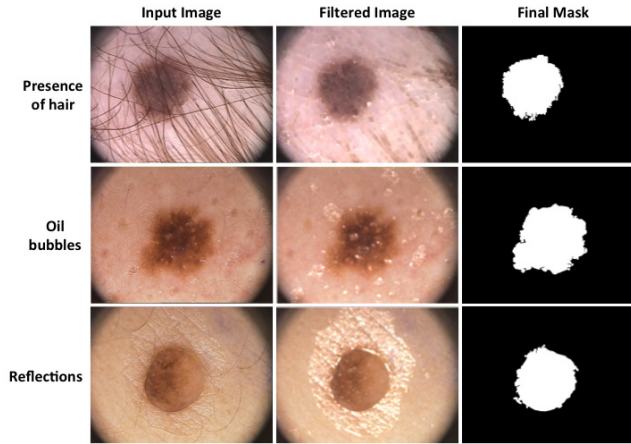Figure 3: Functional architecture of the ASLM method.

7

Figure 4: Artifact removal: original input image, filtered image, and final mask.

It is possible to test ASLM on-line by uploading any dermoscopic image through the web service available at: `www.dis.uniroma1.it/~pennisi/` `skin_lesion_segmentation`

3.1. Artifact Removal and Image Equalization

The RGB dermoscopic image I in input is processed through a morphological transformation in order to remove hair, thus obtaining a new RGB image F (called filtered image). The morphological transformation aims at removing the outlier pixels that can be introduced in the image acquisition phase, while preserving the visual properties of the lesion region.

In particular, F is the result of a closing operation with an $11{\times}11$ kernel having each element $e_{ij} = 1$. The size of the kernel has been selected with the following considerations. Given that the diameter of a hair varies from 17 to 180 μm [28] and the PH^2 image size is $768{\times}574$ pixels, it follows that the average diameter of a hair in a PH^2 image corresponds to about 5 pixels. Thus, by using a $11{\times}11$ kernel, it is possible to close the pixels of the hair with the pixels of its surrounding area and to preserve the shape of the lesion. The closing operation is performed on the three RGB color channels of I separately.

The artifact removal process tends to highlight reflections and air/oil bubbles in the image, but this does not influence the final mask (see Fig. 4). The filtered image F, coming from the artifact removal phase, is processed
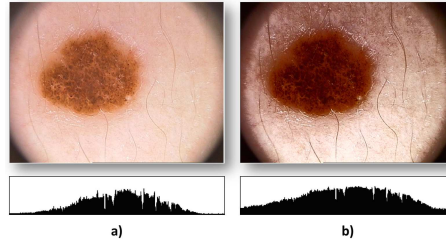
8

Figure 5: Image equalization process. a) Input image and the corresponding luminance spectrum before equalization. b) Equalized Image: the luminance spectrum is modified.
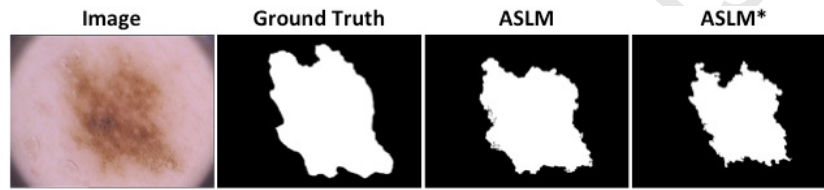

Figure 6: An example of binary masks generated with (ASLM) and without (ASLM*) equalization. Equalization can improve the segmentation accuracy.

to get an equalized image E. The equalization step, performed by applying the OpenCV[1] function *equalizeHist* on the Y channel, helps in highlighting the lesion borders and in obtaining a more accurate output, since the color difference between the lesion area and the surrounding skin are stressed (see Fig. 5). As a demonstration of the importance of equalization for ASLM, an example where the binary masks generated with and without equalization are compared is shown in Fig. 6. The mask generated by using equalization has a higher segmentation accuracy. The image E is used as input for both the parallel processes of Skin Detection and Lesion Segmentation.

3.2. Skin Detection

After equalization, pixels belonging to the skin are identified. A number of methods for skin segmentation in color images are available in the literature. The simplest methods define boundaries in the chosen color space for identifying skin clusters. The main advantage of such methods is that they do not require a training phase. However, it is difficult to define the boundaries that give good results by considering a single color space only [29]. For
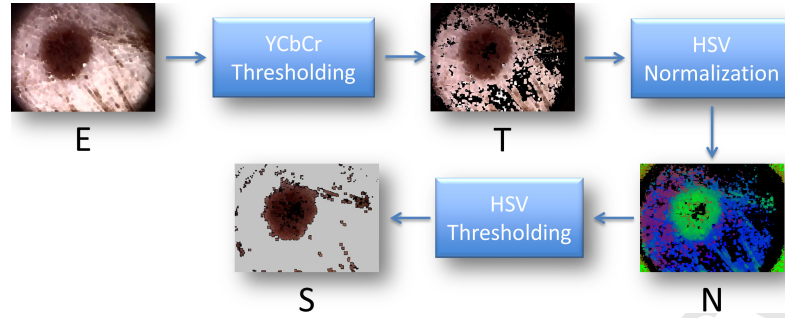
---

[1]www.opencv.org

9

Figure 7: Skin detection process.

Algorithm 1: Skin Detection

Input: RGB equalized image E;
  thresholds: $th_{cb} = 127$, $th_{cr} = 145$, $th_h = 160$, $th_v = 15$
Output: HSV image S
Data structures: YCrCb images E' and T; HSV images Z and N

$E' \leftarrow RGBtoYCrCb(E)$
initialize $\forall\ i, j\ T(i,j) = < 0, 0, 0 >$
foreach $< y, cr, cb > pixel\ E'(i,j)$ **do**
$\quad$ **if** $(cr \le th_{cr}) \wedge (cb \le th_{cb})$ **then**
$\quad\quad$ $T(i,j) \leftarrow < y, cr, cb >$

$Z \leftarrow YCrCbtoHSV(T)$
foreach $< h, s, v > pixel\ Z(i,j)$ **do**
$\quad$ $h' \leftarrow h/(h+s+v)$
$\quad$ $s' \leftarrow s/(h+s+v)$
$\quad$ $v' \leftarrow v/(h+s+v)$
$\quad$ $N(i,j) \leftarrow < h', s', v' >$

initialize $\forall\ i, j\ S(i,j) = < 0, 0, 0 >$
foreach $< h, s, v > pixel\ N(i,j)$ **do**
$\quad$ **if** $(h \le th_h) \wedge (v \le th_v)$ **then**
$\quad\quad$ $S(i,j) \leftarrow < h, s, v >$

---

such a reason, in our ASLM algorithm, we adopt a combination of multiple color spaces.

The main steps in the skin detection process are shown in Fig. 7, while Algorithm 1 provides the details. E is converted into the YCrCb color space and the skin region is detected by using a thresholding on the luminance and chrominance values, producing an image T. YCrCb has been chosen for two

10

1
2
3
4
5
6
7
8
9
10

Algorithm 2: Lesion Segmentation

Input: RGB equalized image E;
      thresholds: $\sigma = 5, min\_canny\_1 = 0.03, max\_canny\_1 = 2.0, \omega = 0.5$
Output: HSV image L
Data structures: RGB image Q; grayscale image G; binary image C; set of
  triangles $< x, y, z >$ D, set of tuples $< a, l, x, y, z >$ R

$Q \leftarrow GaussianBlurring(E, \sigma)$
$G \leftarrow RGBtoGray(Q)$
$C \leftarrow CannyEdgeDetection(G, min\_canny\_1, max\_canny\_1)$
$D \leftarrow DelaunayTriangulation(C)$
initialize $\forall \ i, j \ L(i,j) = < 0, 0, 0 >$; $l = 0$
foreach *triangle* $t :< x, y, z > \in D$ **do**
    $a = \frac{1}{n} \sum_{p=1}^{n} (h_p + s_p + v_p)$ where p is an HSV pixel $\in t$ with values (h_p, s_p, v_p)
    and n is the total number of pixels in t
    $R \leftarrow R \cup < a, l, x, y, z >$
    $l \leftarrow l + 1$
foreach *pair of adjacent tuples* $r_1 :< a_1, l_1, x_1, y_1, z_1 >$ *and*
$r_2 :< a_2, l_2, x_2, y_2, z_2 > \in R$ **do**
    if $(|a_1 - a_2| \leq \omega)$ **then**
        $l_2 \leftarrow l_1$

---

²²³ reasons: 1) it is good for skin detection through thresholding [29] and 2) the
²²⁴ luminance component does not influence skin segmentation in YCrCb [30].

²²⁵ However, considering the YCrCb color space only is not sufficient for
²²⁶ obtaining accurate results, since illumination variations and shadows can
²²⁷ generate false positive detections. This is why T is converted into the HSV
²²⁸ color space and then normalized to form a new image N. Subsequently, N
²²⁹ is further filtered by applying a second thresholding, this time on the HSV
²³⁰ values, thus obtaining an HSV image S, which contains the lesion area only,
²³¹ with the skin region filtered out. The YCrCb and HSV threshold values
²³² can be predefined depending on the skin type of the analyzed images. The
²³³ threshold values used in ASLM are $th_{cb} = 127$, $th_{cr} = 145$, $th_h = 160$, and
²³⁴ $th_v = 15$, which are suitable for skin colors varying from white to cream
²³⁵ white.

²³⁶ *3.3. Lesion Segmentation*

²³⁷ The process of extracting the contours of the lesion area is shown in
²³⁸ Algorithm 2. It is derived from the method proposed in [31] and comprises
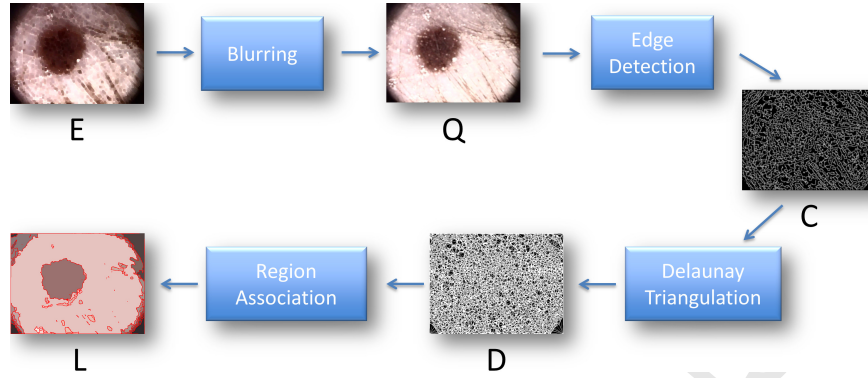²³⁹ four main steps (see Fig. 8).

11

Figure 8: Image Segmentation process.

The image E is filtered along the Red, Green and Blue channels separately by a Gaussian blur filter with a kernel size $\sigma = 5$. The resulting images are merged to create a new RGB image Q, which is a blurred version of E. Then, Q is converted to grayscale and the Edge Detection procedure begins with a Canny edge extraction, which leads to the creation of a grayscale image C containing the intensity edges in Q. The two parameters min_canny_1 and max_canny_1 in the Canny algorithm have been set to the values 0.03 and 2.0 respectively, in order to focus on short edges in the input image. The detected edges are then vectorized into connected line segments — generated as described in [32] — and passed as input for the Delaunay Triangulation procedure, which computes a triangular tessellation of the image.

The Delaunay Triangulation of a point set $\mathfrak{P}$ is characterized by the empty circumdisk property: no point in $\mathfrak{P}$ lies in the interior of any triangle's circumscribing disk.

Definition [33]. *In the context of the finite point set $\mathfrak{P}$, a triangle is Delaunay if its vertices are in $\mathfrak{P}$ and its open circumdisk is empty (i.e., it contains no point in $\mathfrak{P}$). It is worth noting that any number of points in $\mathfrak{P}$ can lie on a Delaunay triangle's circumcircle. An edge is Delaunay if its vertices are in $\mathfrak{P}$ and it has at least one empty open circumdisk. A Delaunay Triangulation of $\mathfrak{P}$, denoted Del $\mathfrak{P}$, is a triangulation of $\mathfrak{P}$ in which every triangle is Delaunay.*

The connected line segments are passed as input to the *Delaunay* function
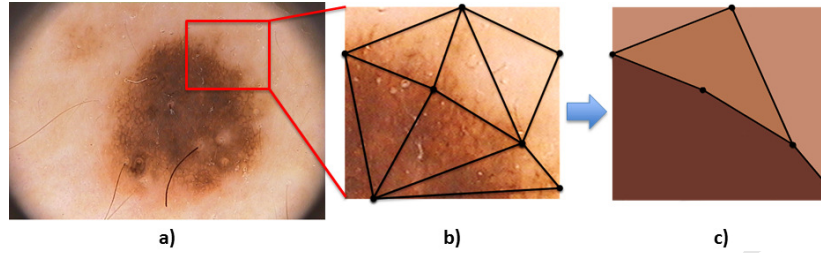
12

Figure 9: Delaunay Triangulation. a) Input image from the PH^2 database [11, 12]. b) Detail of the Delaunay Triangulation. c) Resulting polygons after the association step.

of the CGAL^2 library, in order to carry out the triangulation. The nodes of the planar triangular graph obtained from the triangulation represent the set of triangles, while the edges indicate adjacency relations between them, i.e., there is an edge between two nearby triangles. Deriving a triangular graph from an edge map has two remarkable properties [34]:

1. The triangle boundaries conform to the extracted edges by construction;
2. The tessellation naturally adapts to the content in the images.

This means that large triangles are produced in homogeneous regions of the image, where few edges are detected, while small triangles are generated in the regions where the number of edges is high.

The triangular graph is segmented by using a *Region Association* procedure, which iteratively finds and associates the two regions with the lowest normalized boundary cost, by considering a predefined association threshold ω. In particular, each of the triangles in the graph is considered in turn, by calculating the average HSV color of all the pixels that lie within its circumcircle: If a pair of triangles have a similar HSV value, then they are fused to obtain a new geometric figure. The output of the fusion process between two or more triangles is a polygon made by the union of the fused similar triangles (see the example in Fig. 9). The value for the association threshold ω has been set to 0.5, after measuring the segmentation accuracy on a set of 30 randomly selected samples (10 common, 10 atypical, and 10 melanoma) from PH^2, with ω varying within the range $[0.2, 0.9]$ (see Fig. 10).
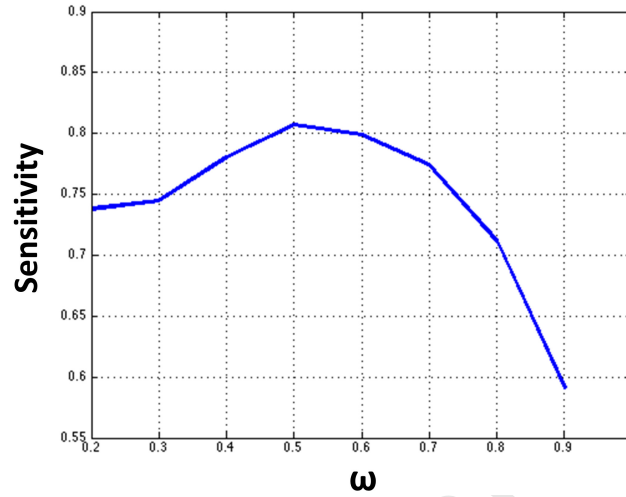
---

^{2}www.cgal.org

13

Figure 10: Value for threshold ω. The curve is obtained by measuring the sensitivity on a set of 30 randomly selected images from PH^2.

The C++ source code for the image segmentation procedure is available on-line at: www.dis.uniroma1.it/~pennisi/fhis.html

3.4. Merging

The final step in the ASLM method concerns merging the results generated by the two parallel processes of Skin Detection and Lesion Segmentation (see Algorithm 3). The idea is that a correctly extracted lesion blob from a binary mask can be circumscribed by a circle with a diameter equal to the major axis of the detected blob. First, the merging procedure detects if one (or more lesion areas) is (are) present in each image S and L. To this end, S and L are converted into binary images (called S_B and L_B, respectively) by assigning the value 255 to the pixels having color values different from the HSV value $<0,0,0>$. In presence of multiple lesion areas, only the biggest blob is considered.

Then, the probabilistic Hough transform is applied to each one of the two images, in order to obtain the number of circles that can be inscribed or circumscribed to the skin lesion area. We adopt the OpenCV function *HoughCircles* with the inverse ratio of resolution $d_p = 1.0$, the minimum distance between detected centers $min_{dist} = 90$ pixels, and the thresholds for the internal Canny detector $min\_canny\_2 = 10$ and $max\_canny\_2 = 255$, which are good parameters to detect long edges.

14

1
2
3
4
5
6
7
8
9
10
11
12
13
14
15
16
17
18
19
20
21
22
23
24
25
26
27
28
29
30
31
32
33
34
35
36
37
38
39
40
41
42
43
44
45
46
47
48
49
50
51
52
53
54
55
56
57
58
59
60
61
62
63
64
65

Algorithm 3: Merging

Input: HSV images S and L; **thresholds:** inverse ratio resolution $d_p = 1.0$,
  minimum distance between detected centers $min_{dist} = 90$, Canny
  thresholds $min\_canny\_2 = 10$ and $max\_canny\_2 = 255$

Output: binary image B

Data structures: Binary images S_B and L_B; number of detected circles n_S and
 n_L

$S_B \leftarrow HSV2Binary(S)$
$L_B \leftarrow HSV2Binary(L)$
$n_S \leftarrow HoughCircles(S_B, d_p, min_{dist}, min\_canny\_2, max\_canny\_2)$
$n_L \leftarrow HoughCircles(L_B, d_p, min_{dist}, min\_canny\_2, max\_canny\_2)$
if $n_S \neq 0$ *and* $n_L \neq 0$ **then**
 $\quad \lfloor \ B \leftarrow AND(S_B, L_B)$
else if $n_S \neq 0$ **then**
 $\quad \lfloor \ B \leftarrow S_B$
else if $n_L \neq 0$ **then**
 $\quad \lfloor \ B \leftarrow L_B$

---

305   Three cases are possible:

306   1. One or more detected circles in S_B and one or more in L_B. Then, B is
307   the result of the pixel-wise logical AND of S_B and L_B.

308   2. One or more detected circles in S_B, but no detections in L_B. Then,
309       $B = S_B$.

310   3. No detections in S_B, but one or more detected circles in L_B. Then,
311       $B = L_B$.

312   Fig. 11 shows three examples for the merging procedure. The first row
313 illustrates an example where a circle can be detected both in S_B and L_B,
314 thus the final image B is the pixel-wise logical AND of the two images. It
315 can happen that the skin detection process generates an S_B image where
316 *HoughCircles*, by using the predefined parameters, cannot find any circle
317 (see the second row). However, since a circle can be detected in the L_B
318 image, then $B = L_B$. The third row shows an example where the final image
319 B corresponds to S_B, since no circles can be detected in L_B by applying
320 *HoughCircles*. It is worth noting that, for all the 200 images in the PH^2
321 database, it was always possible to find at least a circle in one of the two
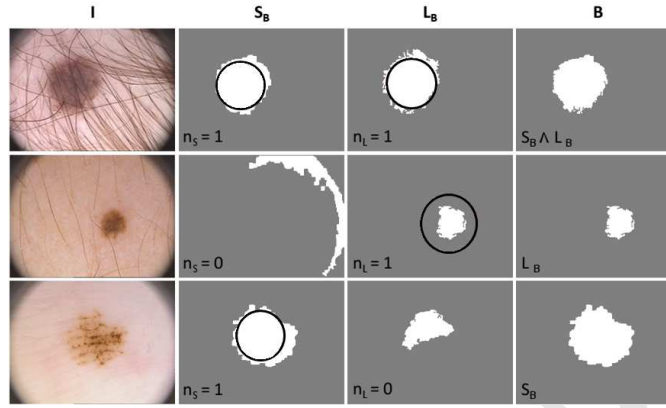322 images S_B and L_B by using the above listed parameters.

15

Figure 11: The results of the skin detection and the lesion segmentation processes are merged to obtain the final binary image B. Images are from the PH^2 database [11, 12].

4. Experimental Results

The experimental validation for the ASLM method has been conducted on a publicly available database of dermoscopic images, containing ground truth annotations. In such a way, the ASLM performance can be quantitatively compared with other existing skin lesion segmentation algorithms. The aim of this section is to show that 1) ASLM demonstrates good segmentation capacity on dermoscopic images in average; 2) When benign lesions are processed, ASLM has particularly high performance; 3) Only when malignant lesion are considered, the segmentation results are less accurate. This behavior is very interesting since, as discussed in Section 5, it can be exploited for melanoma detection.

4.1. Data Set Description

The PH^2 database [11, 12] has been realized by the Universidade do Porto, Tecnico Lisboa in collaboration with the Hospital Pedro Hispano in Matosinhos, Portugal. The database is composed of 200 RGB dermoscopic images, with a resolution of 768×574 pixels and a magnification of 20×, annotated with ground truth data. The 200 images are divided into benign lesions (80 common and 80 dysplastic nevi) and malignant lesions (40 melanomas), with a skin color that varies from white to cream white, i.e., type II and III according to the Fitzpatrick skin type classification scale [35].

For each image, the ground truth data include the following information:
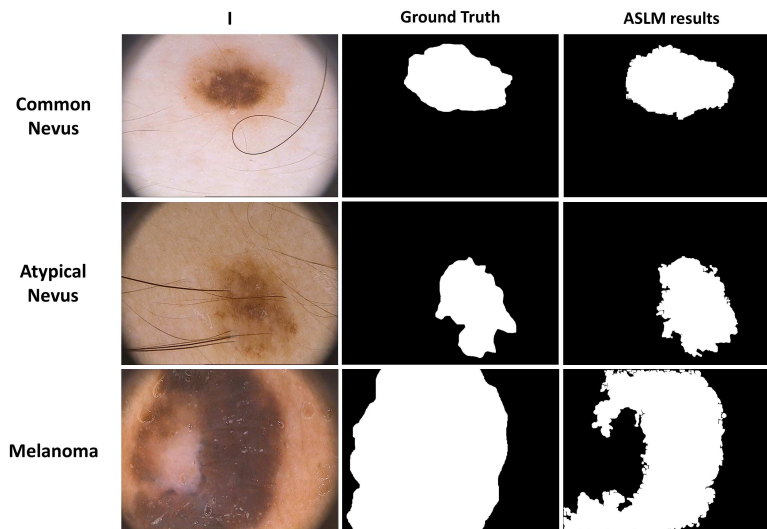
16

Figure 12: ASLM results on PH^2 images IMD046 (common nevus, first row), IMD048 (atypical mole, second row) and IMD058 (melanoma, third row).

- A ground truth binary image, manually generated by expert dermatologists, containing the skin lesion area;

- Clinical and histological diagnosis;

- Dermoscopic criteria.

In particular, in the provided ground truth binary image, the pixels with value 1 belong to the segmented lesion, while pixels with value 0 correspond to the background. Dermoscopic criteria include asymmetry, colors, pigment network, dots/globules, streaks, regression areas, and blue-whitish veil.

4.2. Qualitative Analysis

All the 200 images in the PH^2 database have been segmented using ASLM method with the same parameters and can be downloaded at: `www.dis. uniroma1.it/~pennisi/skin_lesion_segmentation/results.zip`
Three examples of application for the ASLM skin lesion segmentation algorithm are shown in Fig. 12: in the first row a common nevus is shown, in the second row an atypical mole, and in the third row a melanoma. It is worth noting that, for the images in the first and second rows of Fig. 12, the binary images obtained by ASLM are: 1) in very good accordance with

17

Table 1: List of the fully-automatic and semi-automatic methods used for the comparison. For each method, the used implementation is cited.

Method	Fully-Automatic	Category
JSEG [36]	NO	region-based
SRM [37]	NO	region-based
KPP (MATLAB 2014a)	NO	thresholding
K-means (OpenCV 2.4)	NO	thresholding
Otsu (MATLAB 2014a)	YES	thresholding
Level Set [38]	YES	contour-based
ASLM	YES	region-based

361 respect to the corresponding ground truth images in PH^2 and 2) the results
362 are not affected by the presence of hair.

363   A situation where ASLM provides a binary image containing an under-
364 estimated lesion area is shown in the third row of Fig. 12: This is an in-
365 teresting behavior of ASLM algorithm when dealing with melanoma images,
366 which is discussed in the next section.

367 *4.3. Quantitative Analysis*

368   In order to carry out a quantitative evaluation of the ASLM algorithm,
369 we took into account six well-known segmentation methods, namely JSEG,
370 SRM, KPP, K-means, Otsu, and Level Set, which have been already con-
371 sidered for skin lesion images [8, 16]. All the above listed approaches have
372 been used for skin lesion segmentation in dermoscopy images and they can
373 be classified according to the categories provided in Section 2.

374   It is important to underline that, since we were unable to find the original
375 source code, we relied on publicly available third-party implementations of
376 the considered six methods, maintaining the default parameters. This means
377 that the experimental results can change if the original implementations are
378 used. The references to the used implementations are given in Table 1. As
379 a difference with the JSEG, SRM, and KPP lesion segmentation methods
380 reported in the literature, not all the six considered implementations are fully-
381 automatic, four of them (i.e., JSEG, SRM, KPP, and K-means) requiring an
382 active interaction with the user to select the regions of interest.

383   Four different metrics have been selected to calculate the segmentation
384 results: *sensitivity*, *specificity*, *accuracy*, and *F-measure*. The definitions for
385 the used metrics are given in the following equations, where TP is the number

18
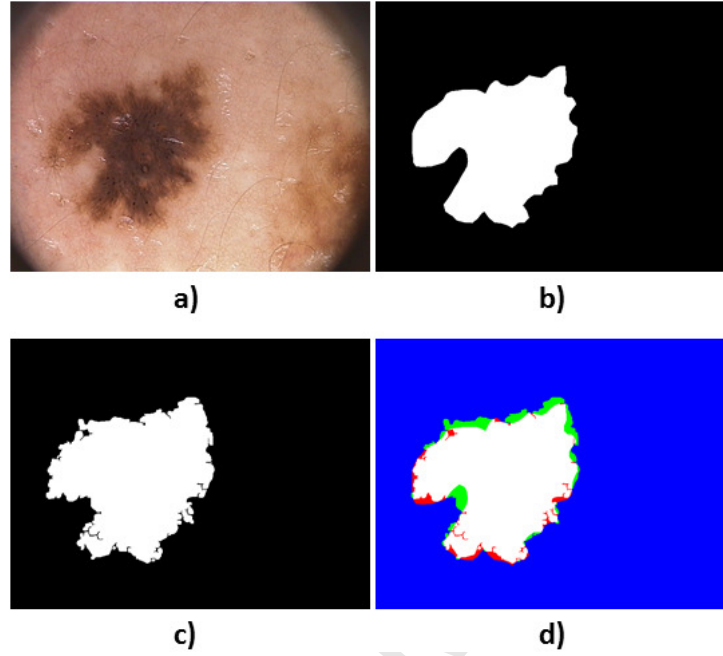
Figure 13: a) IMD043 dermoscopic image from PH^2 database. b) Ground truth provided in PH^2. c) Binary mask produced by ASLM. d) Error evaluation: White pixels are true positives (TP), blue pixels are true negatives (TN), pixels red are false negatives (FN) and green pixels are false positives (FP).

386 of true positive pixels, FP is the number of false positive pixels, TN is the
387 number of true negative pixels, and FN is the number of false negative pixels
388 (see Fig. 13). The chosen metrics are widely used in the literature to measure
389 the performance of skin lesion segmentation methods [39].

$$Sensitivity = \frac{TP}{TP + FN} \tag{1}$$

$$Specificity = 1 - \frac{TN}{TN + FP} \tag{2}$$

$$Accuracy = \frac{TP + TN}{TP + FN + TN + FP} \tag{3}$$

$$F\text{-}measure = \frac{1}{n} \sum_{i=1}^{n} 2 \frac{Prec_i \times Rec_i}{Prec_i + Rec_i} \tag{4}$$

19

Table 2: Skin lesion segmentation results on 200 images from the PH^2 dermoscopic image database.

Method	Sensitivity	Specificity	Accuracy	F-measure
JSEG	0.7108	0.9714	0.8947 ± 0.0176	0.7554
SRM	0.1035	0.8757	0.6766 ± 0.0346	0.1218
KPP	0.4147	0.9581	0.7815 ± 0.0356	0.5457
K-means	0.7291	0.8430	0.8249 ± 0.0107	0.6677
Otsu	0.5221	0.7064	0.6518 ± 0.0203	0.4293
Level Set	0.7188	0.8003	0.7842 ± 0.0295	0.6456
ASLM	**0.8024**	**0.9722**	$\mathbf{0.8966 \pm 0.0276}$	**0.8257**

where n is the total number of images and:

$$Rec_i(P) = TP_i/(TP_i + FN_i) \qquad Prec_i(P) = TP_i/(TP_i + FP_i)$$
$$Rec_i(N) = TN_i/(TN_i + FP_i) \qquad Prec_i(N) = TN_i/(TN_i + FN_i)$$
$$Rec_i = (Rec_i(P) + Rec_i(N))/2 \qquad Prec_i = (Prec_i(P) + Prec_i(N))/2$$

390   Table 2 shows the segmentation results obtained by considering the com-
391 plete PH^2 data set (200 images). ASLM achieves the best performance with
392 respect to the other considered segmentation algorithms on all the used evalu-
393 ation metrics. Moreover, the only comparable results on accuracy and speci-
394 ficity are obtained by JSEG — we have considered the implementation in
395 [36]. It is important to point out that, in the computation of the experimen-
396 tal measures, JSEG has been used as a semi-automatic method, manually
397 merging, in case of over-segmentation, the correctly detected lesion regions.
398 ASLM is a fully-automatic method and no adjustments to the generated
399 binary mask have been performed.

400   Since the dermoscopic images in PH^2 are labeled according to their med-
401 ical diagnosis, it is possible to carry out a finer analysis, by considering
402 separately the three diagnostic classes (common nevi, atypical moles, and
403 melanomas). Table 3 shows the segmentation results that are obtained when
404 processing the 80 images of common nevi only. It can be noted that, for
405 the ASLM method, the sensitivity increases from 0.8024 to 0.8717, the accu-
406 racy raises from 0.8966 to 0.9477, and the F-measure becomes 0.8690 from
407 0.8257. This means that the ASLM algorithm achieves very good results in
408 segmenting images of common nevi.

409   The same behavior can be observed by considering the segmentation per-

20

Table 3: Skin lesion segmentation results on 80 melanocytic nevi (common healthy lesions) images from the PH^2 dermoscopic image database.

Method	Sensitivity	Specificity	Accuracy	F-measure
JSEG	0.6977	**0.9783**	0.9370 ± 0.0027	0.7265
SRM	0.0751	0.9332	0.7250 ± 0.0277	0.0611
KPP	0.3360	0.9566	0.7912 ± 0.0241	0.3960
K-means	0.7008	0.8767	0.8466 ± 0.8467	0.6004
Otsu	0.4777	0.7832	0.6911 ± 0.0193	0.3658
Level Set	0.7069	0.8262	0.7996 ± 0.0264	0.5856
ASLM	**0.8717**	0.9760	$\mathbf{0.9477 \pm 0.0032}$	**0.8690**

Table 4: Skin lesion segmentation results on 80 dysplasic nevi (atypical moles) images from the PH^2 dermoscopic image database.

Method	Sensitivity	Specificity	Accuracy	F-measure
JSEG	0.7435	0.9708	0.9236 ± 0.0065	0.7768
SRM	0.1042	0.8954	0.6812 ± 0.0358	0.0919
KPP	0.2895	0.9446	0.7512 ± 0.0261	0.3568
K-means	0.7650	0.8804	0.8501 ± 0.0065	0.6914
Otsu	0.5515	0.7579	0.6779 ± 0.0193	0.4372
Level Set	0.7364	0.8237	0.7985 ± 0.0346	0.6532
ASLM	**0.8640**	**0.9733**	$\mathbf{0.9271 \pm 0.0099}$	**0.8689**

Table 5: Skin lesion segmentation results on 40 melanoma (malignant lesions) images from the PH^2 dermoscopic image database.

Method	Sensitivity	Specificity	Accuracy	F-measure
JSEG	0.6746	0.9593	$\mathbf{0.7591 \pm 0.0456}$	**0.7710**
SRM	0.2234	0.7512	0.4148 ± 0.0366	0.2852
KPP	0.2648	0.7623	0.4324 ± 0.0336	0.3589
Otsu	0.5971	0.4870	0.5524 ± 0.0211	0.6064
Level Set	0.7073	0.7015	0.7249 ± 0.0214	0.7503
K-means	**0.7141**	0.7010	0.7313 ± 0.0230	0.7550
ASLM	0.5404	**0.9597**	0.6615 ± 0.0506	0.6524

⁴¹⁰ formance on the 80 images of atypical moles only (see Table 4). In such
⁴¹¹ a case, the ASLM method performs better than the other six considered

21

Table 6: Average computational time per image applying the ASLM algorithm on the whole PH^2 database.

Image Size	i3-2370M 4GB avg. ms	i5-3320M 4GB avg. ms	i7-4760HQ 16GB avg. ms
768×574	1990.68	1826.31	1151.1

methods on all the used metrics. In particular, the sensitivity for ASLM method increases from 0.8024 to 0.8640, the accuracy raises from 0.8966 to 0.9271, and F-measures achieves 0.8689 from 0.8257. Thus, even in the case of dysplasic lesions (i.e., atypical moles), which are benign lesions, the ASLM algorithm obtains very good segmentation results.

On the other hand, a strong decrease in the quality of the segmentation results can be observed, on the totality of the used metrics, when only images containing melanomas are processed (see Table 5). In particular, ASLM presents the larger decrease among all the considered methods in the average accuracy, which becomes rather low (i.e., 0.6615) when compared to the accuracy obtained on all the PH^2 images (i.e., 0.8024 — see Table 2).

Summarizing, ASLM achieves a very high accuracy when dealing with benign lesions, namely common nevi and atypical moles, while the accuracy decreases when melanoma images are processed.

4.4. Run-time Performance

The average milliseconds (ms) needed by ASLM for generating a single binary image has been measured by considered all the 200 images in the PH^2 database. The results obtained with three different CPUs are shown in Table 6, demonstrating that the proposed approach can achieve a remarkable speed with commercial CPUs. We used a single-thread C++ implementation and better results can be obtained by adopting a multi-thread version. In particular, the skin detection and the lesion segmentation processes can be parallelized.

5. Using ASLM Binary Masks for Classification

The analysis of the segmentation results generated by evaluating the three classes of nevi separately leads to the following considerations:
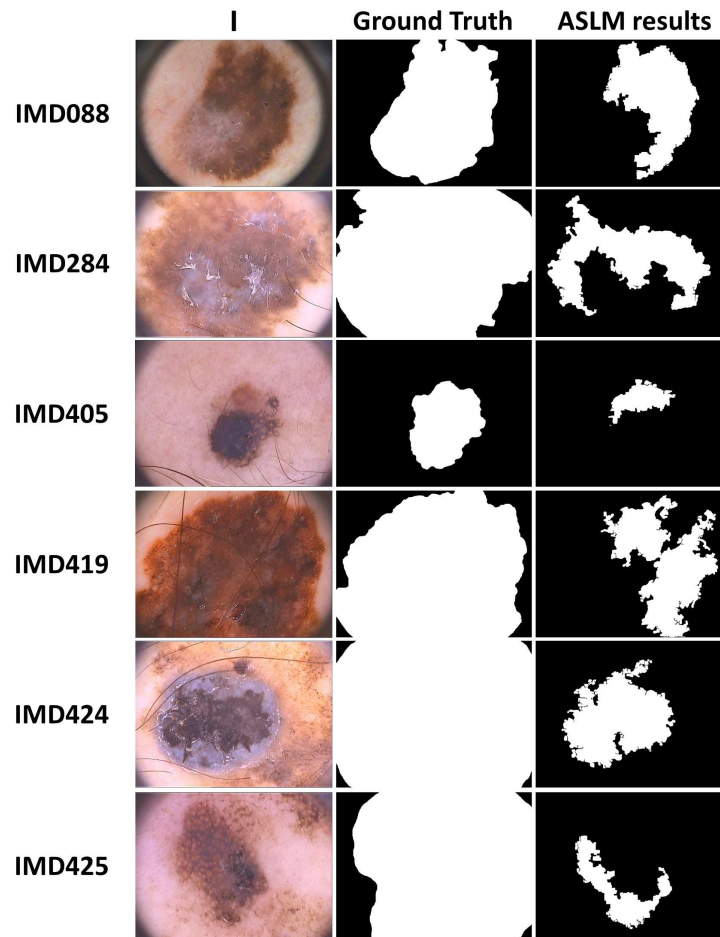
22

Figure 14: ASLM results on PH^2 melanoma images IMD088 (streaks, regression areas, blue-whitish veil), IMD284 (blue-whitish veil, second row), IMD405 (blue-whitish veil), IMD419 (blue-whitish veil), IMD424 (streaks, blue-whitish veil), and IMD425 (regression areas, blue-whitish veil).

1. For benign lesions (i.e., common and atypical nevi), the average accuracy is rather high (0.9477 and 0.9271, respectively);

2. For malignant lesions (i.e., melanoma images), the accuracy significantly decreases (0.6615).

This means that only in the case of malignant lesions the ASLM algorithm gives less accurate results.

Examples of ASLM under-segmentation results in case of melanoma images are shown in Fig. 14, where images containing streaks, regression areas,

23

and blue-whitish veil are considered. A possible motivation for this behavior can be found in the studies described in [40] and in [41]. In those studies emerge that the presence of light brown structureless areas in atypical melanocytic lesions maybe very useful in differentiating atypical nevi from melanomas. According to [40], particular attention is needed to melanocytic lesions that, over time, reveal a loss of network in favor of structureless areas and exhibit new colors such as dark brown, black, gray, blue, red, and white. Homogeneous areas and light brown structureless regions were the most sensitive and specific epiluminescence microscopy features for thin melanomas [41]. Since the ASLM algorithm is based on a color region merging procedure for computing the segmentation results, it is strongly sensitive to structureless areas and homogeneous regions with a color different from the surrounding one.

5.1. Feature Extraction

In order to understand if the binary masks generated by ASLM can be employed for classification purposes, three features have been considered to represent the geometric properties of the detected lesion region:

- *Convex Area*: Scalar that specifies the number of pixel of the convex hull that contains the binary image;

- *Filled Area*: Scalar specifying the number of lesion pixels in the binary image with all holes filled in.

- *Solidity*: Scalar specifying the proportion of the pixels in the convex hull that are also in the region. It is computed as $Area/ConvexArea$.

The above listed features have been selected since they can be used to measure the border irregularity. Fig. 15 shows the results obtained by plotting the normalized values of Filled Area against Convex Area for the 200 binary masks. The majority of melanoma images (red circles) deviate from the distribution of the non-melanoma ones (blue triangles). Fig. 16 shows the results obtained by plotting the normalized values of Filled Area against Solidity: Non-melanoma samples (blue triangles) are concentrated in the top-left part of the diagram. Fig. 17 shows the results obtained by plotting the normalized values of Solidity against Convex Area, with non-melanoma samples (blue triangles) grouped in the top-left corner.
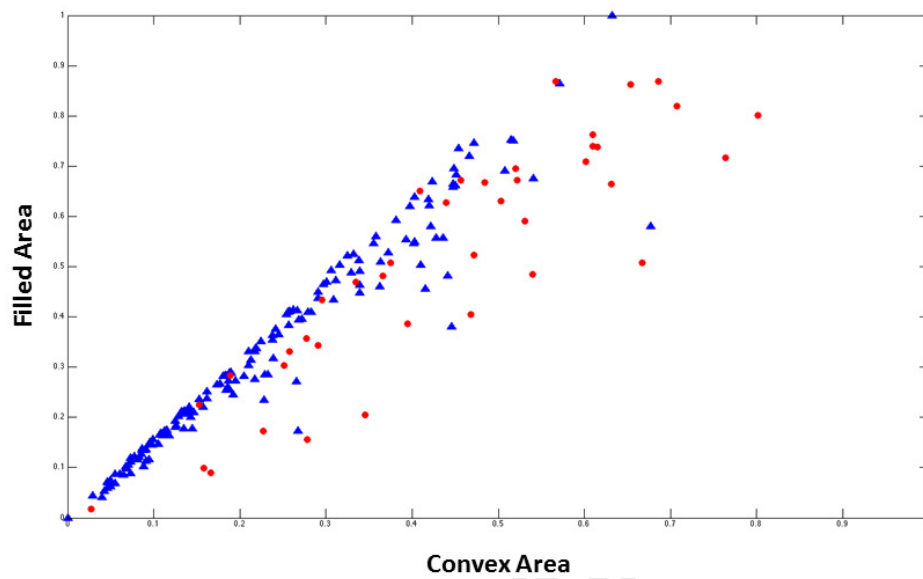
24

Figure 15: Filled Area plotted against Convex Area. Melanoma images are represented as red circles and benign lesion images (common and atypical nevi) as blue triangles.
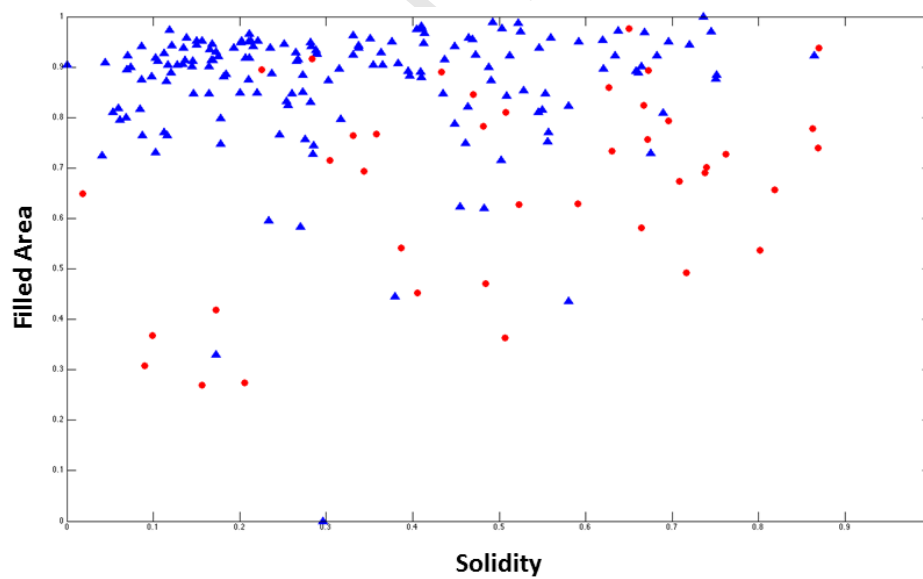

Figure 16: Filled Area plotted against Solidity. Melanoma images are represented as red circles and benign lesion images (common and atypical nevi) as blue triangles.
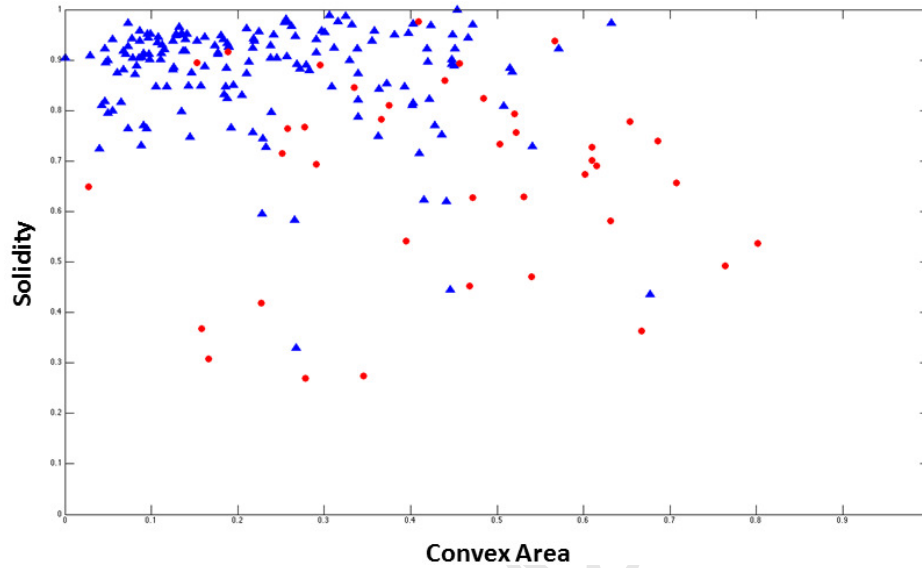
25

Figure 17: Solidity plotted against Convex Area. Melanoma images are represented as red circles and benign lesion images (common and atypical nevi) as blue triangles.

479   In addition to the three above described geometrical features, three 16-
480 bin color histograms for each dermoscopic image are computed. The first
481 histogram of 16 bins represents the distribution of the normalized hue (H)
482 values extracted from the original dermoscopic image I by using the binary
483 image B as a mask. Each bin i, $0 \leq i \leq 15$, contains the number of pixels
484 from $I \wedge B$ in the range $[16*i, 16*i+15]$, normalized with respect to the total
485 number of pixels of $I \wedge B$ (see Fig. 18). The second and the third histograms
486 contain the values for V and S, respectively, calculated in the same way of
487 the H values.

488 *5.2. Classification Results*

489   For classifying the binary masks, we decided to train four classifiers: (i)
490 Naive Bayes, (ii) Adaboost, (iii) K-Nearest Neighbors (KNN), and (iv) Ran-
491 dom Trees. The classifiers take as input a feature set made of the above listed
492 geometrical and color properties. We selected the aforementioned classifier
493 since they are preferred when the number of images in each class varies.

     We tested the proposed classification methods by adopting the implemen-
tation provided by Weka [42] and a leave-one-out approach: The classifiers
are trained by using all the images except one, which is used for testing.
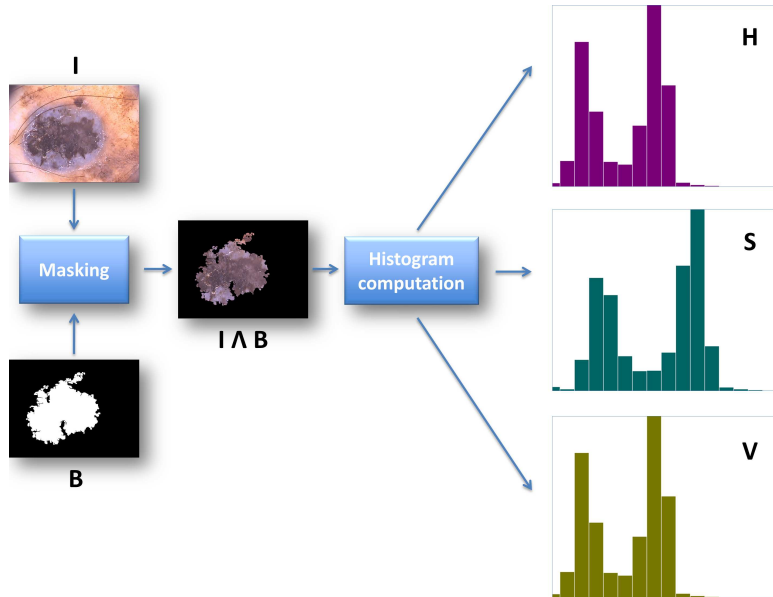
26

Figure 18: Three normalized color histograms are computed in the HSV color space for each image in the data set by using the binary images generated by ASLM as masks.

Then, the process is repeated by changing the test image. The parameters of each classifier have been automatically chosen by Weka. The metrics selected for calculating the goodness of the classification process have been: *sensitivity*, *specificity*, *precision*, and *F-measure*. Sensitivity, Specificity and F-measure have been computed as described in Section 4, while Precision, that represents the fraction of retrieved instances that are relevant, has been calculated as follows:

$$Precision = \frac{TP}{TP + FP} \tag{5}$$

The obtained results, reported in Table 7, show that by analysing the binary masks generated by ASLM it is possible to achieve good results in terms of classification. The Adaboost classifier, thanks to the characteristic of combining rough and moderately inaccurate rules of thumb, obtains a sensitivity of about 93.5% and a specificity of 87.1%. This classifier is based on the observation that finding many rough rules of thumb can be easier than finding a single one, thus obtaining a highly accurate classifier. Adaboost classifier is able to correctly recognize 153 over 160 benign lesions and 34 over 40 melanoma images.

27

Table 7: Classification with Naive Bayes, KNN, Adaboost, and Random Trees classifiers.

Classifier	Sensitivity	Specificity	Precision	F-measure
KNN	0.875	0.706	0.872	0.873
Bayes	0.825	0.806	0.863	0.836
Adaboost	**0.935**	**0.871**	**0.936**	**0.935**
Random Trees	0.890	0.804	0.895	0.892

503 The Naive Bayes classifier considers the contribution of each feature as
504 being independent of the correlation probability between the single feature
505 and the rest of the considered features. Moreover, it also achieve good results
506 when the number of images in each class varies. In our case, the classifier
507 can correctly classify 32 over 40 images of malignant lesions, obtaining a
508 sensitivity of 82.5% and a specificity of 80.6%.

509 The KNN and the RT classifiers are based on the majority vote approach,
510 which is influenced by the distribution of the features. For this reason, the
511 feature distribution influences the classification performance. The KNN clas-
512 sifier correctly classifies 26 over 40 melanoma images, with a sensitivity of
513 87.5% and a specificity of 70.6%. The RT classifier presents 89.0% sensitivity
514 and 80.4% specificity, with 31 over 40 melanomas correctly recognized.

515 These preliminary classification results, obtained by considering only three
516 geometrical features (i.e., convex area, filled area, and solidity) and three 16-
517 bin color histograms, are promising and allow to consider the use of ASLM
518 as a suitable tool for the development of CAD support systems for melanoma
519 detection.

6. Summary and Conclusions

521 In this paper, an automatic skin lesion image segmentation method, de-
522 signed to deal with multiple types of lesion shapes, size and colors, and the
523 presence of hair and air/oil bubbles, has been presented. The proposed al-
524 gorithm, called ASLM, is fully-automatic, it does not require any training
525 stage, and it is computationally fast. ASLM uses different parameters to
526 carry out the segmentation, however most of them are related to the size
527 of the images in input and to the considered skin types, thus they can be
528 predefined.

529 ASLM has been experimentally evaluated on publicly available data from

28

the PH^2 dermoscopic image database [11, 12], in order to allow a quantitative comparison with other existing segmentation techniques. Furthermore, the source code of our lesion segmentation algorithm is publicly available and we also provide a web service to test ASLM on-line by freely loading dermoscopic images.

The quantitative analysis of the performance of our method has been carried out by considering four different quality metrics. The results demonstrate that ASLM can achieve better accuracy in extracting the portion of the dermoscopic image containing the skin lesion compared to six well-known image segmentation algorithms. Moreover, the ASLM method shows an interesting behavior when applied on the images from the PH^2 database: The segmentation results are in very good accordance with ground truth data only when images of benign lesions, namely common and dysplastic nevi, are considered, while the segmentation accuracy decreases considerably when ASLM is applied to images of malignant lesions (i.e., melanomas). This behavior can be explained by the the presence in malignant lesion images of streaks, regression areas, and blue-whitish veil. Indeed, the ASLM algorithm is strongly sensitive to structureless areas and homogeneous regions with a color different from the surrounding one and it generates a binary mask that presents a lesion area that is smaller than the actual one.

The particular ASLM characteristic of being sensitive to images containing irregular borders (which is often the case of reticular pattern and atypical network in melanoma images), brown globules/black dots irregularly arranged at the periphery, pseudopods and radial streaming (bulbous and finger-like projections seen at the edge a lesion), inspired us to use geometrical features of the binary masks generated by ASLM as input for a binary classifier, obtaining promising results. In particular, the classification experiments achieved a sensitivity of 93.5% and a specificity of 87.1% on a set of 200 dermoscopic images with a leave-one-out cross-validation.

Although non suitable for diagnostic applications, the obtained classification results represents, in our opinion, a relevant starting point to further develop an automated analysis. Furthermore, since the segmentation errors made by ASLM, when dealing with melanoma images, can be visually detected, the ASLM method can be suitable to be used as part of a computer-aided diagnosis (CAD) system.

29

References

[1] P. Roma, I. Savarese, A. Martino, and D. et al. Martino. Slow-growing melanoma: Report of five cases. *Journal of Dermatological Case Reports*, 1(1), 2007.

[2] A. J. Miller and M. C. Mihm. Melanoma. *New England Journal of Medicine*, 355(1):51–65, 2006.

[3] D. Meckbach, J. Bauer, A. Pflugfelder, and F. Meier et al. Survival according to braf-v600 tumor mutations an analysis of 437 patients with primary melanoma. *Plos one*, 9(1):1–10, 2014.

[4] E. Cesareo, L. Korkina, G. D'Errico, G. Vitiello, M. S. Aguzzi, F. Passarelli, J. Z. Pedersen, and A. Facchiano. An endogenous electron spin resonance (esr) signal discriminates nevi from melanomas in human specimens: A step forward in its diagnostic application. *PLoS ONE*, 7, 2012.

[5] V. Verdoliva, C. Senatore, M. L. Polci, and S. et al. Rossi. Differential denaturation of serum proteome reveals a significant amount of hidden information in complex mixtures of proteins. *PLoS ONE*, 8, 2013.

[6] S. Bassoli, A. Maurichi, M. Rodolfo, A. Casari, and et al. CDKN2A and MC1R variants influence dermoscopic and confocal features of benign melanocytic lesions in multiple melanoma patients. *Exp. Dermatol.*, 22(6):411–6, 2013.

[7] M. Mete and N. M. Sirakov. Dermoscopic diagnosis of melanoma in a 4D space constructed by active contour extracted features. *Comp. Med. Imag. and Graph.*, 36(7):572–579, 2012.

[8] P. Wighton, T. K. Lee, H. Lui, D. I. McLean, and M. S. Atkins. Generalizing common tasks in automated skin lesion diagnosis. *Information Technology in Biomedicine, IEEE Transactions on*, 15(4):622–629, 2011.

[9] F. Xie and A. C. Bovik. Automatic segmentation of dermoscopy images using self-generating neural networks seeded by genetic algorithm. *Pattern Recognition*, 46(3):1012–1019, 2013.

30

[10] M. E. Celebi, Q. Wen, S. Hwang, H. Iyatomi, and G. Schaefer. Lesion border detection in dermoscopy images using ensembles of thresholding methods. *Skin Research and Technology*, 19(1):e252–e258, 2013.

[11] T. Mendonca, P. M. Ferreira, J. S. Marques, A. R. Marcal, and J. Rozeira. Ph^2 - a dermoscopic image database for research and benchmarking. *Conf Proc IEEE Eng Med Biol Soc*, 2013:5437–5440, 2013. http://www.fc.up.pt/addi/ph2

[12] J. L. Garcìa Arroyo and B. Garcìa Zapirain. Detection of pigment network in dermoscopy images using supervised machine learning and structural analysis. *Computers in Biology and Medicine*, 44:144 – 157, 2014.

[13] A. Pennisi, D. D. Bloisi, D. Nardi, A. R. Giampetruzzi, C. Mondino, and A. Facchiano. Melanoma detection using delaunay triangulation. In *IEEE 27th International Conference on Tools with Artificial Intelligence*, pages 791–798, 2015.

[14] M. E. Celebi, H. Iyatomi, G. Schaefer, and W. V. Stoecker. Lesion border detection in dermoscopy images. *Computerized Medical Imaging and Graphics*, 33(2):148 – 153, 2009.

[15] M. E. Celebi, Q. Wen, H. Iyatomi, K. Shimizu, H. Zhou, and G. Schaefer. *A State-of-the-Art Survey on Lesion Border Detection in Dermoscopy Images*, pages 97–129. CRC Press, 2015.

[16] M. Silveira, J. C. Nascimento, J. S. Marques, and A. R. et al. Marcal. Comparison of segmentation methods for melanoma diagnosis in dermoscopy images. *J. Sel. Topics Signal Processing*, 3:35–45, 2009.

[17] G. Sforza, G. Castellano, S.A Arika, and LeAnder et al. Using adaptive thresholding and skewness correction to detect gray areas in melanoma in situ images. *IEEE Transactions on Instrumentation and Measurement*, 61(7):1839–1847, 2012.

[18] R. Garnavi, M. Aldeen, M. E. Celebi, G. Varigos, and S. Finch. Border detection in dermoscopy images using hybrid thresholding on optimized color channels. *Computerized Medical Imaging and Graphics*, 35(2):105 – 115, 2011.

31

[19] H. Zhou, Mei Chen, Le Zou, R. Gass, L. Ferris, L. Drogowski, and J.M. Rehg. Spatially constrained segmentation of dermoscopy images. In *5th IEEE International Symposium on Biomedical Imaging: From Nano to Macro*, pages 800–803, 2008.

[20] H. Iyatomi, H. Oka, M. E. Celebi, M. Hashimoto, M. Hagiwara, M. Tanaka, and K. Ogawa. An improved internet-based melanoma screening system with dermatologist-like tumor area extraction algorithm. *Comp. Med. Imag. and Graph.*, 32:566–579, 2008.

[21] B. Erkol, R. H. Moss, R. J. Stanley, W. V. Stoecker, and E. Hvatum. Automatic lesion boundary detection in dermoscopy images using gradient vector flow snakes. *Skin Res Technol*, 11(1):17–26, 2005.

[22] H. Zhou, X. Li, G. Schaefer, M. E. Celebi, and P. Miller. Mean shift based gradient vector flow for image segmentation. *Computer Vision and Image Understanding*, 117:1004–1016, 2013.

[23] J. C. Nascimento and J. S. Marques. Adaptive snakes using the em algorithm. *IEEE Trans Image Process*, 14(11):1678–1686, 2005.

[24] T. F. Chan and L. A. Vese. Active contours without edges. *IEEE Transactions on Image Processing*, 10(2):266–277, 2001.

[25] Y. Deng and B. S. Manjunath. Unsupervised segmentation of color-texture regions in images and video. *IEEE Transactions on Pattern Analysis and Machine Intelligence*, 23(8):800–810, 2001.

[26] R. Nock and F. Nielsen. Statistical region merging. *IEEE Trans. Pattern Anal. Mach. Intell.*, 26:1452–1458, 2004.

[27] M. E. Celebi, H. A. Kingravi, H. Iyatomi, and Y. A. et al. Aslandogan. Border detection in dermoscopy images using statistical region merging. *Skin Research and Technology*, 14(3):347–353, 2008.

[28] B. Ley. Diameter of a human hair. http://www.webcitation.org/mainframe.php, 1999.

[29] F. Gasparini and R. Schettini. Skin segmentation using multiple thresholding. In *Internet Imaging VII, IS&T/SPIE Electronic Imaging*, volume 6061, pages 60610F–1, 60610F–8. SPIE, 2006.

32

[30] S. L. Phung, A. Bouzerdoum, and D. Chai. Skin segmentation using color pixel classification: analysis and comparison. *Pattern Analysis and Machine Intelligence, IEEE Transactions on*, 27(1):148–154, 2005.

[31] C. J. Taylor and A. Cowley. Parsing indoor scenes using rgb-d imagery. In *Proceedings of Robotics: Science and Systems*, pages 401–408, 2012.

[32] Q. Wu and Y. Yu. Two-level image segmentation based on region and edge integration. In *Digital Image Computing: Techniques and Applications*, pages 957–966, 2003.

[33] S.-W. Cheng, T. K. Dey, and J. Shewchuk. *Delaunay mesh generation*. CRC Press, 2012.

[34] C. J. Taylor and A. Cowley. Segmentation and analysis of rgb-d data. In *RSS 2011 Workshop on RGB-D Cameras*, pages 1–2, 2011.

[35] T. B. Fitzpatrick. Ultraviolet-induced pigmentary changes: Benefits and hazards. *Current Problems in Dermatology*, 15:25–38, 1986.

[36] Q. Zhao. JSEG method implementation. `cs.joensuu.fi/~zhao/Software/JSEG.zip`, 2001.

[37] S. Boltz. SRM method implementation. `www.mathworks.com/matlabcentral/fileexchange/authors/73145`, 2010.

[38] R. Crandall. Level set implementation. `https://github.com/rcrandall/ChanVese`.

[39] A. Madooei, M. S. Drew, M. Sadeghi, and M. S. Atkins. Automated pre-processing method for dermoscopic images and its application to pigmented skin lesion segmentation. *Color and Imaging Conference*, 2012(1):158–163, 2012.

[40] V. Terushkin, S. W. Dusza, A. Scope, and G. Argenziano et al. Changes observed in slow-growing melanomas during long-term dermoscopic monitoring. *The British Journal of Dermatology*, 166(6):1213–1220, 2012.

33

[41] G. Annessi, R. Bono, F. Sampogna, T. Faraggiana, and D. Abeni. Sensitivity, specificity, and diagnostic accuracy of three dermoscopic algorithmic methods in the diagnosis of doubtful melanocytic lesions. *Journal of the American Academy of Dermatology*, 56(5):759–767, 2007.

[42] I. H. Witten and E. Frank. *Data Mining: Practical Machine Learning Tools and Techniques, Second Edition*. Morgan Kaufmann, 2005.

34

Authors' Biographies

Andrea Pennisi is Post-doctoral researcher at Vrije Universiteit Brussels (VUB), Belgium. He received his Ph.D. and M.Sc. in Computer Engineering from Sapienza University of Rome in 2015 and 2010, respectively, and his B.Sc. in Computer Engineering from University of Catania, Italy in 2007. His main research interests are related to image segmentation, multi-sensor surveillance, and crowd analysis.

Domenico D. Bloisi is Research Associate at Sapienza University of Rome, Italy. He received his PhD, M.Sc., and B.Sc. degrees in Computer Engineering from Sapienza University of Rome in 2010, 2006 and 2004, respectively. His main research interests are related to image processing, intelligent surveillance (including object detection, visual tracking, and multiple sensor data fusion), and robotics.

Daniele Nardi is Full Professor at Sapienza University of Rome, Italy. His current research interests are mainly in the field of Artificial Intelligence in the area of Knowledge Representation and Reasoning and Multi-agent and Multi-robot systems. He received the IJCAI-91 Publishers Prize for the paper "Tractable Concept Languages", the prize Intelligenza Artificiale from the Associazione Italiana per l'Intelligenza Artificiale (AI*IA) and is ECCAI fellow since 2009. From 2011 to 2014 he has been President of RoboCup and was co-chair of IEEE Technical Committee of International Workshop on Safety, Security and Rescue Robotics.

Anna Rita Giampetruzzi is Medical Doctor and dermatologist with specific interest for cutaneous skin cancers and autoimmune diseases. Since more than twelve years she is engaged in the study of imaging cutaneous and clinical application of non-invasive diagnostic techniques. She is an expert in early diagnosis of melanoma and non-melanoma skin cancers by dermoscopy. Currently, she is involved in a study concerning cutaneous melanoma metastasis.

Chiara Mondino is Senior Medical Doctor at the Department of Dermatology (Service of Allergology and Clinical Immunology), Cantonal Hospital of Bellinzona, Switzerland. She received her M.Sc. at the Faculty of Medicine and Surgery, University of Turin, Italy and her specialization on Allergology and Clinical Immunology from the University of Genoa, Italy. From 2002 to 2014 she has been Senior Medical Doctor and Vice-Director at the Depart-

35

726 ment of Allergology and Immunodermatology at the Istituto Dermatologico
727 dell'Immacolata (IDI) of Rome, Italy.

728 **Antonio Facchiano** is Medical Doctor and oncologist. He has a long
729 experience in the study of molecular mechanisms controlling angiogenesis and
730 cancer growth and he has contributed to the identification of novel anticancer
731 molecules. He is also involved in studies aiming at the identification of novel
732 early markers of melanoma development.

36